

DNS of Surface Textures to Control the Growth of Turbulent Spots

James S. Strand¹ and David B. Goldstein²
The University of Texas at Austin, Austin, TX, 78712

A spectral DNS code was used to study the growth and spreading of turbulent spots in a nominally laminar, zero-pressure gradient boundary layer. In addition to the flat wall case, an investigation was also conducted of the interaction of these spots with riblets, fins, and “spanwise-damping fins”. The flat plate, surface textures, and initial spot perturbation were simulated via an immersed boundary method, and a “suction-wall” allowed the available channel code to model a boundary layer. In all cases, self-similar arrowhead shaped spots formed. A decrease in spreading angle was observed for cases with real fins, with the largest decrease of between 11% and 23% of the flat wall value (depending on the technique used to calculate the angle) corresponding to the most closely spaced fins. The spanwise-damping fins had little effect at the largest spacings. At the lowest spacing, corresponding to the best case of the real fins, the damping fins reduced the spreading angle by 56% to 74% of the flat wall value. The riblets tested here had double the spacing of the most effective fins, but were still able to reduce spot growth by 7% to 10% of the flat wall value.

Nomenclature

U_∞	=	free-stream velocity
U	=	streamwise velocity
V	=	wall-normal (vertical) velocity
W	=	spanwise velocity
δ_o^*	=	boundary layer displacement thickness at the location of the perturbation
δ_o	=	boundary layer 99% thickness at the location of the perturbation
ν	=	kinematic viscosity
η	=	similarity variable for the Blasius solution (see Eq. 2)
h	=	surface texture height
s	=	surface texture crest-to-crest spacing
t	=	time
x	=	streamwise coordinate
y	=	wall-normal coordinate
z	=	spanwise coordinate

I. Introduction

A. Turbulent Spots

Turbulent spots form naturally during the boundary layer transition process. As Tollmien-Schlichting waves in a boundary layer grow to large amplitudes, secondary instabilities develop and turbulent spots form. These spots take on an arrowhead shape, pointing downstream. Emmons¹ was the first to describe these spots, and for this reason they are sometimes referred to as Emmons spots. The spots appear at randomly distributed points and their growth and merging lead to complete transition to turbulence. A spot appears as a fairly well defined region of turbulence surrounded by laminar flow.

Turbulent spots can also be artificially generated with a localized perturbation in a laminar boundary layer. Artificially generated spots have been investigated with both experiments and DNS simulations. Schubauer and

¹ Graduate Researcher, Aerospace Engineering Dept., 1 University Station, C0600, Student.

² Professor, Aerospace Engineering Dept., 1 University Station, C0600, Senior Member.

Klebanoff² studied both naturally occurring and artificially generated spots in a low-disturbance wind tunnel. In order to generate spots artificially, they used an electrical spark for the localized perturbation. Wygnanski et al.³ studied artificially generated spots in greater detail, also with an electrical spark for the perturbation. They found that if the perturbation was not strong enough, it was possible that no spot would develop. However, if a spot did form it exhibited self-similar growth, independent of the initial perturbation. Wave packets, which were identified as TS waves, were observed near the upstream lateral edges of the spot. Wygnanski et al. hypothesized that the breakdown of these wave packets led to the formation of eddies near the spanwise edges of the spot, and thus that the waves were at least partially responsible for the growth of the spots. A distinct overhang region was observed at the leading edge of the spot. Amini and Lespinard⁴ introduced a perturbation by injecting fluid through a hole in the flat plate by means of a loudspeaker. The vertical velocity induced directly above the hole by the injection was as high as $1.25U_\infty$. They were primarily interested in studying a pre-turbulent spot, but their method of perturbation did generate the same arrowhead-shaped turbulent spots as other experiments. Using isodeviation contours of mean velocity, they estimated the spreading angle of the turbulent spot to be $\sim 10^\circ$, and the apex angle to be $\sim 30^\circ$. For a schematic of a turbulent spot, with spreading angle, apex angle, etc. labeled, see Fig. 1.

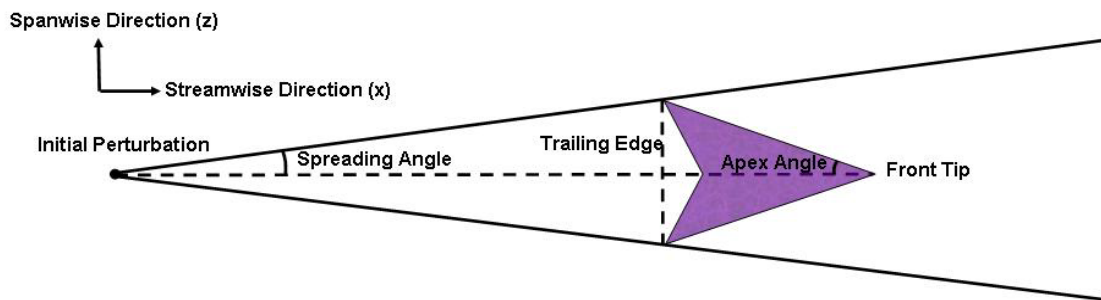


Figure 1. Schematic top view of a turbulent spot

DNS has also been used to simulate turbulent spots. Henningson et al.⁵ used a spectral method to simulate the growth and spreading of a turbulent spot in an incompressible flat plate boundary layer. The domain for these simulations was periodic in the streamwise and spanwise directions. To approximate the effect of the thickening of the surrounding boundary layer as the spot moves downstream, a weak body force was applied. The perturbation used to induce the spot was a localized, impulsive body force directed upstream. The force was Gaussian in space, centered at the wall, with a radius of $\delta_0/3$, where δ_0 is the boundary layer thickness at the perturbation location. The spots generated with this perturbation exhibited self-similar growth, as found by experiments. Henningson et al. state that “The turbulent vortical region grows at a half-angle of about 7° . The region in which the velocity is disturbed is wider, about 10° , in good agreement with experimental results.” It is not clear how they defined the edge of the turbulent vortical region, or how they defined the edge of the disturbed region. It was found that the growth of the spot became self-similar after $tU_\infty/\delta_0 \approx 100$, with a virtual origin at $tU_\infty/\delta_0 \approx 35$ and $x/\delta_0 \approx 15$. The trailing edge of the spot moved at $\sim 0.5U_\infty$, and the leading edge at $\sim 0.83U_\infty$, and Henningson et al. note that these values compare reasonably well with the commonly quoted experimental values of $0.5U_\infty$ and $0.9U_\infty$, respectively. They also observed an overhang region at the leading edge of the spot, which is consistent with the experiments of Wygnanski et al.³

Singer and Joslin⁶ focused their DNS simulations on the development of a turbulent spot in an incompressible, laminar, zero-pressure-gradient boundary layer. Their domain was periodic in the spanwise direction, and they used a buffer-domain in the streamwise direction to allow for a non-reflective boundary condition on the streamwise velocity. Fluid injection through a short streamwise slot was used to perturb the flow and generate the disturbance that grew into the turbulent spot. They note that some of the structures seen very soon after the fluid injection (especially the “U-shaped vortex”, and “necklace vortex”) are probably specific to the method of perturbation. Other structures seen later, such as the “quasi-streamwise vortices” appear to be much more generic, and would likely be a part of any young turbulent spot. Many of these quasi-streamwise vortices initially formed under the legs of other streamwise vortices. The interaction of these quasi-streamwise vortices with high pressure regions near the wall frequently led to an ejection of fluid away from the wall, and thus served as a method of vortex regeneration.

Viscous entrainment of fluid by nearby vortices also led to the formation of new vortices in some cases, and new vortices were sometimes formed due to the rebound of fluid from the wall. Taken together, the above effects caused the disturbance to spread and grow into a young turbulent spot. Singer and Joslin did not observe a wave packet near the wingtips of the spot, which is consistent with the findings of the DNS done by Henningson et al.⁵ Singer and Joslin did not report on the apex angle, spreading angle, or leading and trailing edge speeds for the young spot.

Singer⁷ used a more advanced computer, along with the same code and method used by Singer and Joslin⁶ (described above), to further simulate the growth of the young turbulent spot. The simulated spot shared many characteristics with experimentally observed spots (such as those described by Wygnanski et al.³), including a distinct overhang region and a calm but non-Blasius region in the wake of the spot. As in the DNS by Henningson et al.⁵, no TS waves were observed at the wingtips of the spot. Singer notes that his streamwise domain is only about five times the typical TS wavelength for the simulation Reynolds number. Furthermore, the calculation is run for less than four times the period of the highest frequency TS wave for the simulation Reynolds number. Thus, he argues that TS waves have neither enough time nor enough room to grow and propagate. The spanwise-averaged skin friction coefficient varies widely along the spot centerline, but when this value is averaged over the length of the spot region, the average value is closer to the turbulent value than the laminar one. A spatially averaged velocity profile does not show a distinct logarithmic region, but Singer states that the flow is likely beginning to develop a log layer. Singer notes some inconsistencies in the values which have been found by various experiments and simulations for the leading edge and trailing edge speeds and the spreading angle of turbulent spots. He attributes these inconsistencies primarily to the various methods used to define the edge of the spot. Some researchers have used isodeviation contours of the streamwise velocity to define the spot edge (this is the method used by Amini and Lespinard⁴), while others (such as Henningson et al.⁵) have used specific isosurfaces of vorticity (or some other pertinent quantity). Singer defines the leading and trailing edges of the spot as the farthest downstream and upstream locations, respectively, at which the quantity $\left| \frac{\partial u}{\partial x} \right|$ along the spot centerline is greater than or equal to

an arbitrary threshold value. He notes that this criterion leads to small jump discontinuities in the movement of the leading edge, and larger discontinuities in the movement of the trailing edge. The spanwise edge is defined similarly, except that the edge is defined as the farthest spanwise point (at any x and y location), where the threshold is met. Again, this leads to multiple jump discontinuities, and thus Singer uses linear regression to define the leading edge and trailing edge speeds, and the spreading angle. He calculates a trailing edge speed of $0.63U_\infty$ and a leading edge speed of $0.94U_\infty$. For the spreading angle, he reports values of 3.8° or 6.4° , depending on whether the origin is defined as before or after a particularly large discontinuity in the plot of the spanwise extent of the spot versus the streamwise location of the spanwise edge. Although these values are significantly lower than previously reported experimental values, he argues that this is probably due to the fact that the Reynolds number (based on distance from the perturbation to the measurement location) was about 80,000, which is significantly lower in the simulation than in most experiments (Wygnanski et al.³ took some data at $Re = 120000$, but most of their data was for $Re = 600000$).

B. Delaying Transition

If one could delay or eliminate the onset of transition, the benefits would be appreciable since the viscous drag of a turbulent boundary layer can be four or more times greater than that of a laminar layer. It has been found experimentally⁸ that passive surface textures, e.g. streamwise riblets, can reduce the *turbulent* drag on a surface by five to ten percent. We have confirmed this numerically and have shown that riblets work by damping the near-wall spanwise fluctuations.^{9,10}

If this damping could slow the spanwise spreading of young turbulent spots, riblets might be used to significantly delay the transition to turbulence, since in most engineering applications the breakdown to turbulence occurs through the growth and merging of turbulent spots. Furthermore, the riblets would only need to be present in the transition region, so the expense would be much lower than the expense associated with covering the entire turbulent region with riblet film. We examine L-shaped or fin-shaped riblets. Although fin-shaped riblets are less feasible than triangular riblets in practice due to manufacturing difficulties, they are much simpler to simulate. A wider range of the key parameters (texture height and spacing) can be examined with fins than with triangular riblets, due to grid considerations, and thus they were investigated herein.

We are primarily interested here in body force fields that represent (via the immersed boundary method) some physically realizable surface texture (fins). Goldstein et al.⁹ found that spanwise damping wires and fins (finite regions in which only the spanwise component of velocity is damped) were effective for damping turbulence. These are, of course, not physically realistic, but they might give an idea of the ideal geometry to be used for fins.

II. Numerical Method

A. The Force Field Model and Spectral Approach

There exist several approaches to simulating laminar and turbulent boundary layers over textured surfaces. We have a method for modeling a variety of surfaces in a spectral method simulation.^{9,10,11} Our approach is particularly flexible and has been successfully tested on a range of turbulent flow configurations over passive surface textures and active MEMS-like devices. The spectral code we use is based on the method in Kim, Moin, and Moser¹² (also described by Handler et al.¹³). The geometry of interest here is a developing boundary layer over a flat plate that has a textured surface. Our technique for modeling a virtual surface introduces a localized body force field into the Navier Stokes equations. Our force field is made to adapt to the flow and bring it to a specified velocity on the intended boundary points thereby creating a virtual surface. The spatial development in the normally homogeneous streamwise direction is modeled, as in Goldstein et al.¹⁴, via an absorbing buffer zone (see Fig. 2).

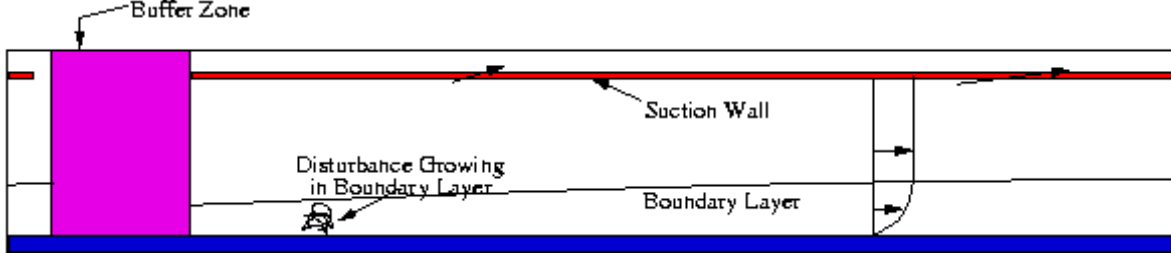


Figure 2. Computational domain with top suction wall to model a Blasius boundary layer

B. Simulation of a Boundary Layer

Before turbulent spots in a boundary layer could be examined, it was necessary for us to modify our channel code to simulate a boundary layer. We use the buffer zone to create the desired inlet Blasius profile. We initially assumed that if the boundary layer was thin compared to the channel height, the top wall of the channel would have very little effect. Unfortunately, this is not the case. The boundary layer did not grow downstream as the Blasius solution would predict. Instead a favorable pressure gradient developed in the streamwise direction, causing the freestream to accelerate significantly. This happened because even when the top wall of the channel was set to allow slip, it still permitted no through flow. There is always some small but finite vertical velocity above a flat plate, even very far from the plate. This velocity can be calculated from the Blasius solution. The vertical velocity at any point in a Blasius boundary layer is given by

$$V = \sqrt{\frac{\nu U_\infty}{2x}} (\eta f' - f) \quad (1)$$

where

$$\eta = y \sqrt{\frac{U_\infty}{2\nu x}} \quad (2)$$

is the similarity variable for the Blasius solution, V is the vertical velocity, and ν is the kinematic viscosity. Here x is the streamwise distance from the leading edge of the flat plate, f is the streamfunction normalized by $\sqrt{2\nu U_\infty x}$, and $f' = \partial f / \partial \eta$.

Note that as η becomes large, $f' \rightarrow 1$, and $(\eta - f) \rightarrow 1.21678$ (for more details, see Ref. 15), so this equation reduces to

$$V = 0.86039 \sqrt{\frac{\nu U_\infty}{x}} \quad (3)$$

In order to model the boundary layer, it was necessary to simulate this vertical velocity. The top wall of the channel cannot be modified to allow through flow, so it was necessary to use an immersed boundary just below the top channel wall to force a suitable upflow. This “suction wall” forces the vertical velocity at each point to be that predicted by the Blasius solution (Fig. 2), thus allowing normal streamwise growth of the boundary layer. Unlike the solid-wall immersed boundaries, the suction wall only applies forces in the vertical direction; it exerts no force in the spanwise or streamwise directions. This suction wall serves the same purpose as a small variation in area in a real wind tunnel, which is used to maintain a zero pressure gradient in a test section. The boundary layer can grow as if from the leading edge of the plate (the plate starts at or near the end of the buffer zone) or the velocity can be set in the buffer zone to a Blasius profile for a given x-location on the plate. In either case the profile will develop correctly downstream.

C. Surface Textures Examined

So far we have investigated spots over four surfaces: a flat wall, riblets, fins, and spanwise damping “fins”. Both the riblets and fins are solid surfaces created with the immersed boundary method. The fins are very simple, they are only one grid node wide, and the only parameters of interest are their height and their spacing. The riblets are somewhat more complex, due to the cosine grid in the normal direction. Also, since the body force is applied at the collocation points, the riblets are slightly stairstepped, rather than completely smooth. If a sufficiently high resolution is used (so that each riblet is at least 5 or 6 grid nodes high), this stairstepping is not a problem. For more detail on how the various immersed boundaries are created, see Ref. 9. Figure 3 is a schematic for the riblet case, and Figure 4 is a similar schematic for the fin case. For clarity, the scale is greatly exaggerated in the wall-normal direction. The buffer zone, quarter-sphere perturbation, and the surface textures are all shown. Only the section of the domain near the bottom wall is shown, the suction wall is located well above the visible area. Note that the spacing and height of the textures can be set as desired for a given simulation. Even in the flat plate case, an immersed boundary is used for the plate, instead of the bottom wall of the channel.

The spanwise damping fins do not bring the flow to rest. Instead, they only apply forces in the spanwise direction, and only the spanwise component of the velocity is forced to zero. Also note that for a given spacing and height the spanwise-damping fins occupy the same space as the regular fins, only the forces applied to the flow are different.

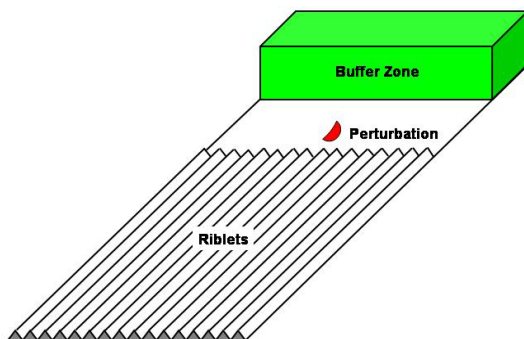


Figure 3. Schematic for riblet case showing 16 riblets, the region of the perturbation, and the buffer zone

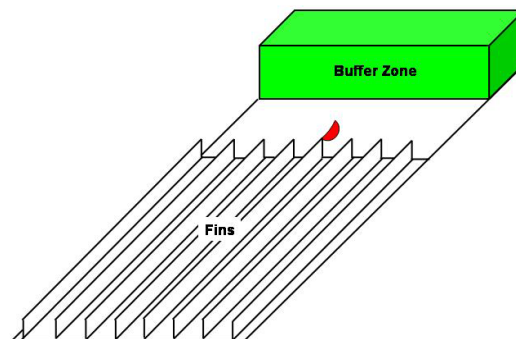


Figure 4. Schematic for the fin case showing 8 fins, the region of the perturbation, and the buffer zone.

When surface textures are used, they begin a short distance downstream from the edge of the buffer zone (as shown in Figs. 3 and 4). They cannot begin inside the buffer zone, or directly at its edge, because the buffer zone has to force a definite profile, and there is no analytic solution for the laminar flow directly above riblets or fins. This means that when the riblets or fins begin, they perturb the flow somewhat. This is, in fact, exactly what would happen in a real experiment if a sheet of riblet film were affixed to a real flat plate. If this leading edge of the textures is too large compared to the boundary layer thickness, it can act as a trip and force the flow turbulent on its own with no other perturbation.

D. Relaxation

When the code is run from a cold start, the streamwise velocity everywhere along the plate is initialized to that of the Blasius profile *for a single x-location*. It is not possible to incorporate the vertical velocity from the Blasius solution, since the top wall of the channel is no-through-flow, and the steady-state velocity profile above the suction wall is not known initially. The spanwise velocity is zero for a Blasius boundary layer. Thus, since the code must satisfy continuity at every time step, initially there can be no variation of streamwise velocity with distance along the plate. It therefore takes a significant amount of time (several flow through times) for a steady state, spatially developing boundary layer to emerge. It is this relaxed profile which provides the initial conditions for the turbulent spot simulations.

E. Initial Perturbation

Several perturbations have been used to generate the spot. The perturbation used for the results presented below is a quarter-sphere bump on the flat plate, with a radius of $0.926 \delta_o^*$, in the region between the end of the buffer zone and the beginning of the textures. The bump is created with the same immersed boundary technique as the plate and the textures. It is made to appear briefly at the beginning of the simulation, and is then removed. If the bump were not removed, a turbulent wedge would be generated instead of a turbulent spot. The bump is deliberately made asymmetric about the spanwise centerline, in order to keep the spot from developing perfect left-right symmetry. Spanwise symmetry is not realistic, as an actual spot is not spanwise symmetric.

F. Defining the Spot

As was discussed previously, there are multiple methods of defining the edges of a turbulent spot. Since one of our primary objectives in this investigation was to determine how various surface textures affect the growth and spreading of spots, it is critical that we use consistent criteria to define our spots. For the current effort two quantities will be used to define spots, enstrophy and vertical velocity. Other quantities will be examined, but when spreading angle, leading edge speed, or trailing edge speed are computed, it will be with these quantities. More than one cutoff value was used for both enstrophy and vertical velocity, and results are reported for each cutoff value. For example, for a given run, the spreading angle may be calculated for as many as four different spot definitions (3 cutoff values for enstrophy, and one for vertical velocity). This will be discussed further when results are presented.

III. Results and Discussion

A. Blasius Profile Verification

Initially, it was necessary to verify that the suction wall method permitted proper spatial development of the boundary layer. In order to check that the boundary layer was growing properly, profiles were examined for several downstream locations, and compared to the Blasius solution. Figure 5 shows the boundary layer profile at the midpoint of the domain in the streamwise direction. The flow is completely uniform in the spanwise direction. The profile corresponds to a position along the plate which is 54.57δ from the leading edge, where δ is the boundary layer 99% thickness at the streamwise location of the profile. Both the streamwise and wall-normal velocity components are shown in the figure, and both compare well with the Blasius solution.

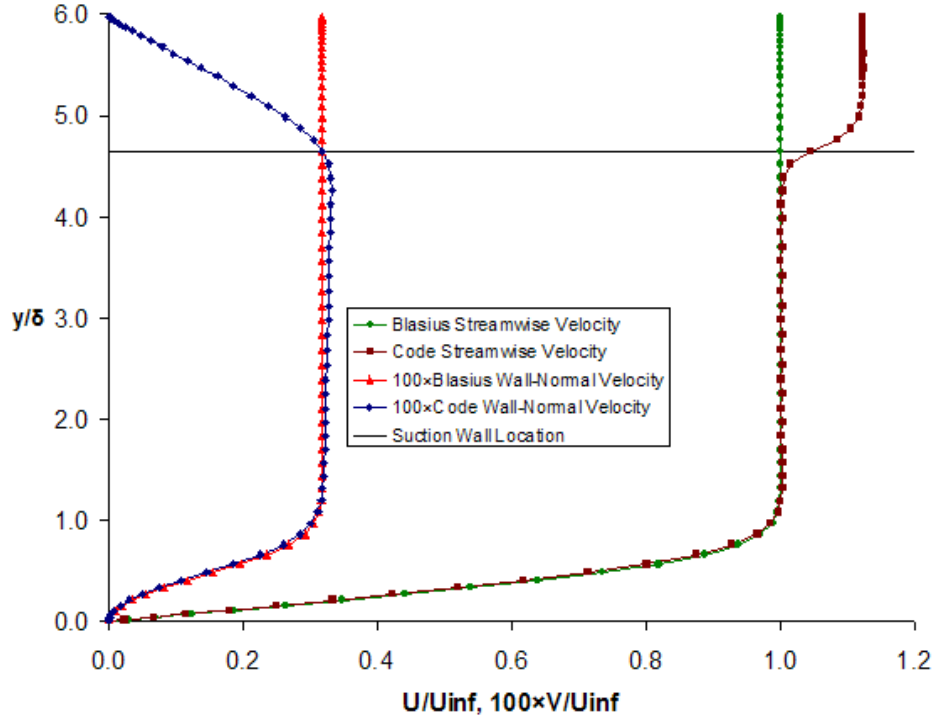
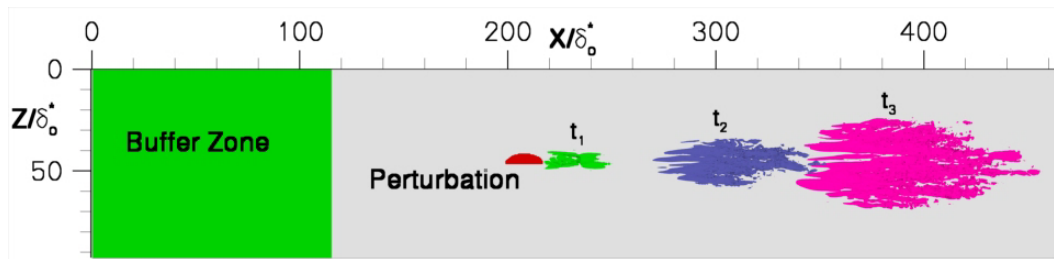


Figure 5. Comparison of the boundary layer profile developed with the suction wall method to that predicted by the Blasius solution midway down the plate. Note that the simulated vertical velocity agrees with the Blasius value right at the suction wall location

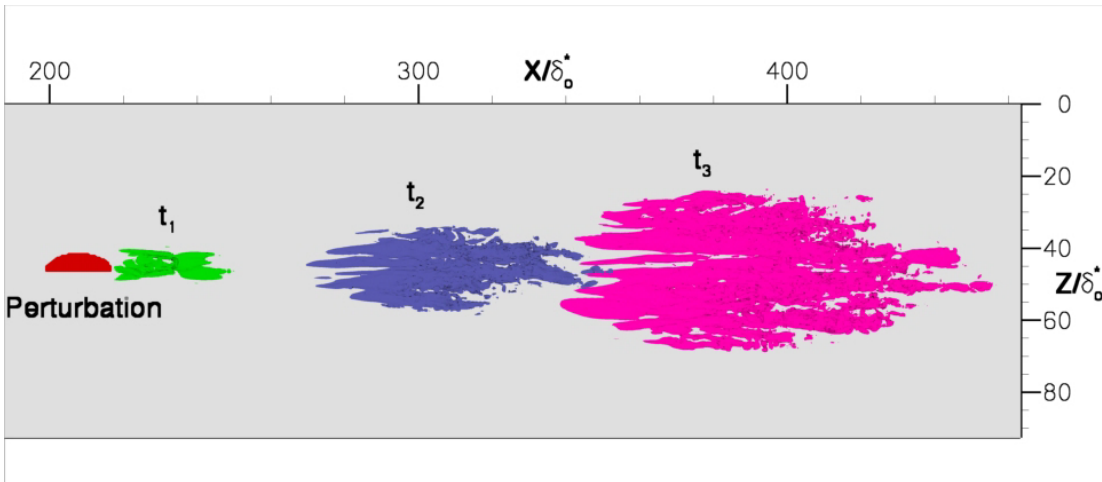
B. Flat Wall

The majority of our runs were performed with a moderately sized domain, which allowed us to capture early spot behavior without overly cumbersome resolution requirements. The domain (see Figs. 2, 3, and 4) had dimensions of $463.2\delta_o^*$, $18.5\delta_o^*$, and $92.6\delta_o^*$ in the streamwise (x), wall-normal (y), and spanwise (z) directions respectively, where δ_o^* is the boundary layer displacement thickness at the location of the perturbation, as calculated from the Blasius solution. For this domain, $512 \times 64 \times 128$ spectral modes were used in the x , y , and z directions, respectively. The perturbation was introduced at $t = 0$ and remained in the flow until $t = 6.95 \delta_o^*/U_\infty$. The spot was followed until $t = 416.9 \delta_o^*/U_\infty$, at which point it reached the end of the streamwise domain (and began to enter the buffer zone). The Reynolds number based on displacement thickness, $Re_{\delta_o^*}$, was 431.8 at the perturbation location. The Reynolds number based on distance from the perturbation to the end of the domain was 109480, which is comparable to the simulations done by Singer⁷.

The flat wall case was run first, to provide a base case for comparison. A top-down view of the flat-wall spot at three different times is shown in Fig. 6. The spot is drawn with isosurfaces of enstrophy at the value of $0.756 U_\infty/\delta_o^*$, and is shown at times $t_1 = 64.5 \delta_o^*/U_\infty$, $t_2 = 208.4 \delta_o^*/U_\infty$, and $t_3 = 347.4 \delta_o^*/U_\infty$. As the spot matures, it takes on the expected arrowhead shape. It is asymmetric about the spanwise centerline, since the perturbation itself is asymmetric. This was done intentionally, in order to prevent the spot from developing with perfect spanwise symmetry, since experimental spots do not have left/right symmetry. Furthermore, such symmetry leads to some unrealistic results, such as zero normal and streamwise vorticity, zero spanwise velocity, and zero helicity on the spot centerline. A quick glance at the figure indicates that the leading edge is moving at a fairly constant speed, since the leading edge moves about the same distance between t_1 and t_2 as it does between t_2 and t_3 .



a.)



b.)

Figure 6. a.) Top view of turbulent spot over a flat wall, drawn with isosurfaces of enstrophy at the value of $0.756 U_\infty/\delta_0^*$ and shown at $t_1 = 64.5 \delta_0^*/U_\infty$, $t_2 = 208.4 \delta_0^*/U_\infty$, and $t_3 = 347.4 \delta_0^*/U_\infty$. b.) Close-up view of the same spot. This run used $512 \times 64 \times 128$ spectral modes in the x , y , and z directions, respectively.

Figure 7 shows a side view of the same flat wall spot, drawn with the same enstrophy isosurface as before, taken at $t = 277.9 \delta_0^*/U_\infty$. The overhang found by the above-referenced experiments and DNS simulations is clearly visible near the leading edge of the spot.

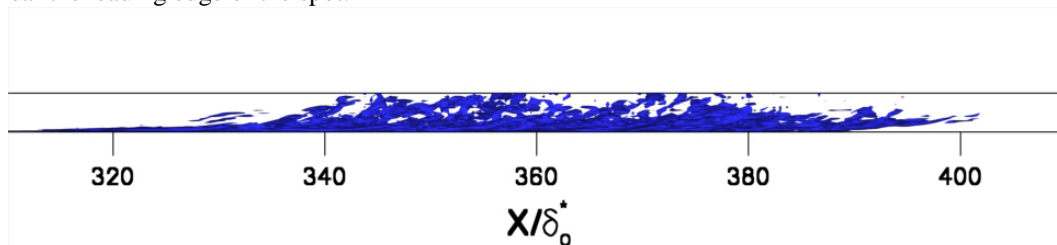


Figure 7. Side view of turbulent spot over the flat wall, drawn with isosurfaces of enstrophy at the value of $0.756 U_\infty/\delta_0^*$ and shown at $t = 277.9 \delta_0^*/U_\infty$. Note the overhang near the leading edge. Also note that only the 20% of the domain closest to the bottom wall is shown, the top of the spot is still far from the suction wall. This run used $512 \times 64 \times 128$ spectral modes in the x , y , and z directions, respectively.

Figure 8 gives a qualitative idea of the spreading angle for the flat wall spot. The 6° angle is drawn simply for comparison; the spreading angle of the flat wall spot is not exactly 6° . The actual spreading angle will be discussed below.

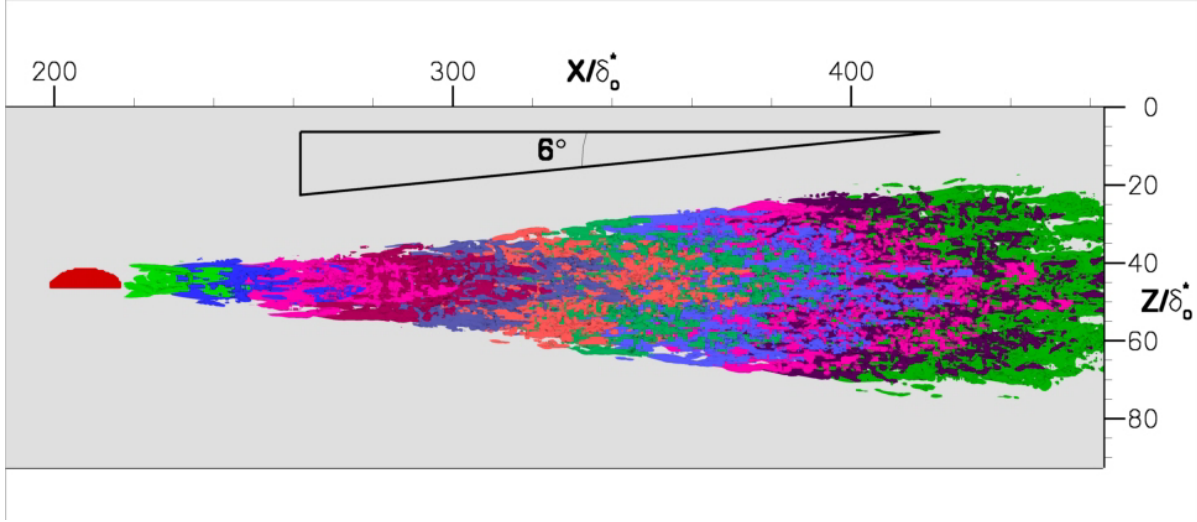


Figure 8. Top view of turbulent spot over a flat wall, drawn with isosurfaces of enstrophy at the value of $0.756 U_\infty/\delta_0^*$. Isosurfaces are shown for multiple time steps simultaneously, in order to illustrate spot spreading angle. This run used $512 \times 64 \times 128$ spectral modes in the x, y, and z directions, respectively.

For comparison, we have run a flat-wall case with double resolution in the spanwise direction. The domain was the same as described above, but for this case $512 \times 64 \times 256$ spectral modes were used in the x, y, and z directions, respectively. Figure 9 is a top-down view of the growth and spreading of the spot, comparable to Fig. 6b and Fig. 8. The spot is similar in shape to the previously described case, but not identical. This may indicate that the original case was somewhat under-resolved, or the differences may be due to the fact that the perturbation is not exactly identical in the two cases, or it may simply be due to the chaotic nature of turbulent flow. In the higher resolution case, the quarter-sphere has the same nominal radius as before, but is smoother, since it is composed of more points. Figure 10 is a zy plane located $359.56\delta_0^*$ from the leading edge of the plate, showing contours of enstrophy, at time $t = 382.1 \delta_0^*/U_\infty$. The spot appears to be composed of a multitude of turbulent mushroom-like structures, and the sliced legs of many streamwise vortices can be seen.

C. Spanwise Damping Fins

We next investigate the spanwise damping fins. Due to the no-slip condition on the streamwise velocity, physically realistic textures (riblets and fins) significantly alter the boundary layer profile near the wall. This means that if the boundary layer profile were averaged in the spanwise direction, the diminished velocity region would extend farther away from the nominal wall location (at the base of the fins or in the valley of the riblets) than it would from a flat wall at the same location. This is not the case with spanwise damping fins, which do not enforce a no-slip condition on the streamwise velocity. Figure 11 shows three zy plane images, one for a flat wall, one for real fins, and one for damping fins. The enstrophy near the wall is almost identical for the flat wall and damping fins cases (on the right side of the images, away from the edge of the spot), but for the real fins case there is a region of very low enstrophy extending up to the tops of the fins, while there are enstrophy concentrations at the tops of the fins.

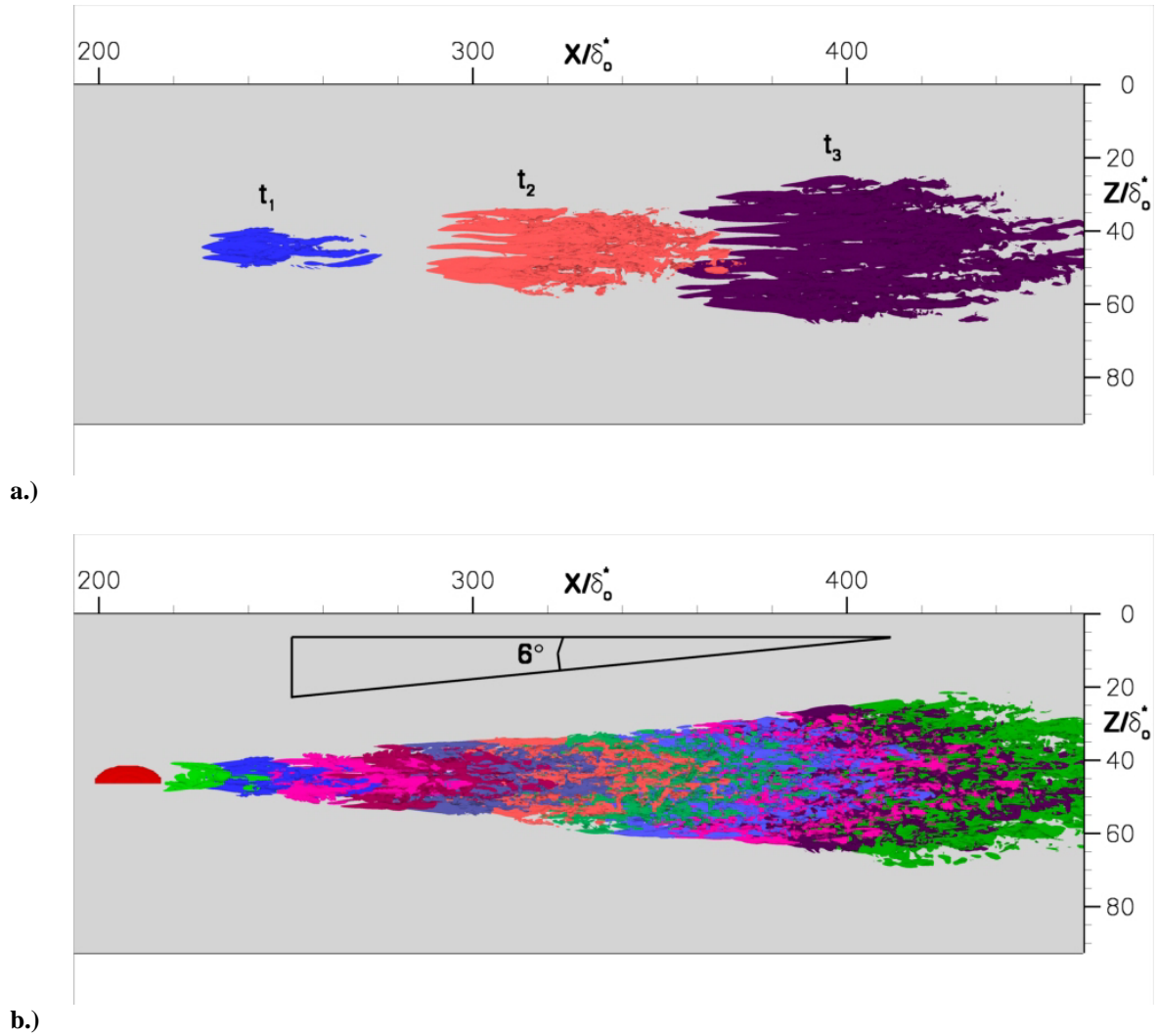


Figure 9. Top view of turbulent spot over a flat wall with double the resolution in the spanwise direction, drawn with isosurfaces of enstrophy at the value of $0.756 U_\infty/\delta_0^*$. a.) Spot shown at $t_1 = 64.5 \delta_0^*/U_\infty$, $t_2 = 208.4 \delta_0^*/U_\infty$, and $t_3 = 347.4 \delta_0^*/U_\infty$. b.) Isosurfaces are shown for multiple time steps simultaneously, in order to illustrate spot spreading angle. This run used $512 \times 64 \times 256$ spectral modes in the x , y , and z directions, respectively.

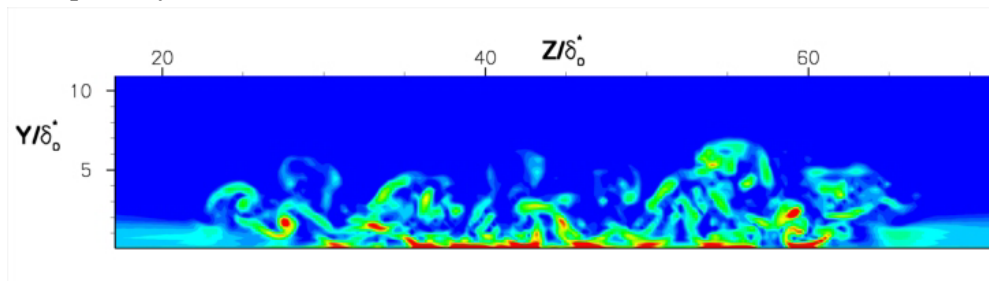


Figure 10. Contours of enstrophy on a zy plane located $359.56\delta_0^*$ from the leading edge of the plate, at time $t = 381.2 \delta_0^*/U_\infty$. This run used $512 \times 64 \times 256$ spectral modes in the x , y , and z directions, respectively.

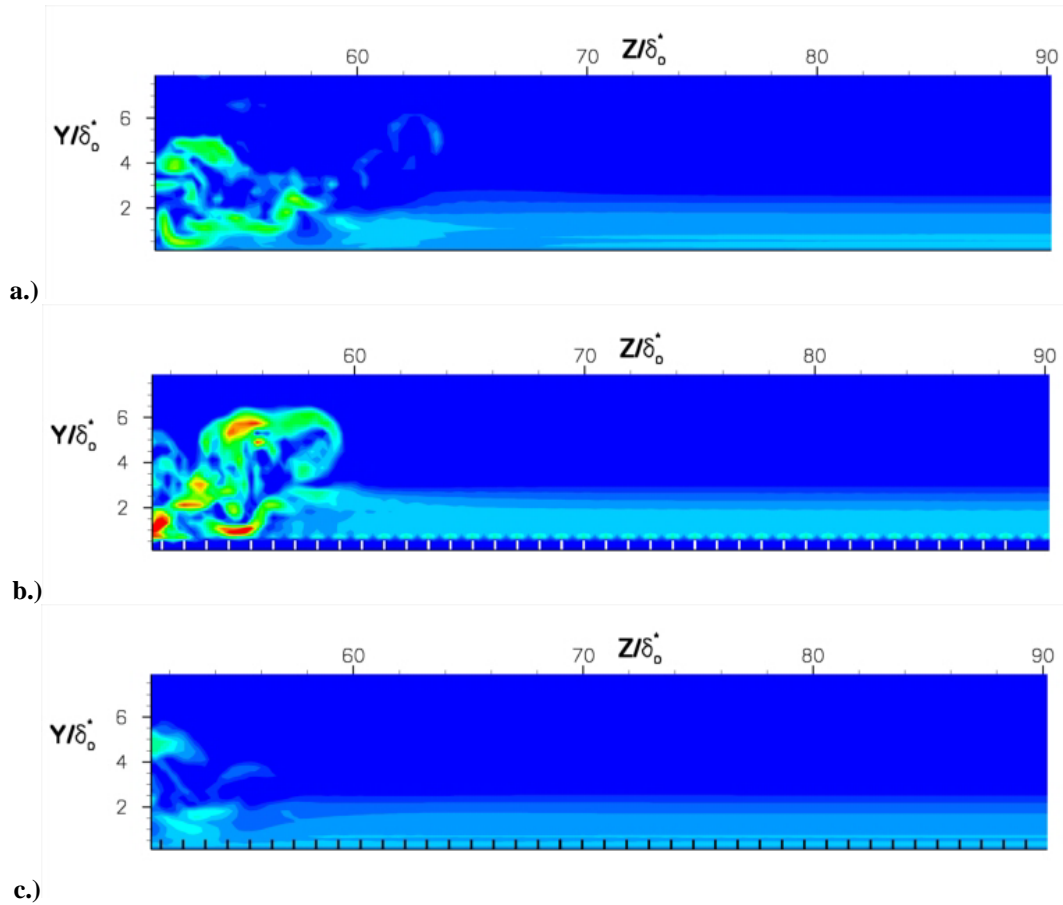


Figure 11. Contours of enstrophy on a zy plane located $360\delta_0^*$ from the leading edge of the plate. Full zy domain is not shown. This run used $512 \times 64 \times 256$ spectral modes in the x , y , and z directions, respectively. a.) Flat wall case. b.) Real fins case. c.) Damping fins case.

The damping fins have no effect on the initial laminar flow. When the flow becomes turbulent, the damping fins can block spanwise velocity fluctuations without inhibiting the streamwise flow. In fact, Goldstein, Handler, and Sirovich⁹ showed that riblets, fins, and damping regions all force the turbulence regions up and away from the wall. Therefore we anticipated that, of the textures studied, the spanwise damping fins would be the most effective for constraining the growth of the spot.

The relevant parameters for the spanwise damping fins are their height and spacing. Reasonable values must be chosen for these parameters if any comparison is to be made between spanwise damping fins and realistic textures. If real fins or riblets are made taller than $\sim\delta_0^*$, we find that they trip the flow turbulent at the abrupt leading edge of the textured region. Spanwise damping fins do not trip the flow, and so can be made as tall as desired. In fact, the damping fins grow more effective at constraining spot growth with increasing height. However, since we are interested primarily in comparing spanwise damping fins to real textures, we have limited ourselves to damping fins with $h < \delta_0^*$. Crest-to-crest spacing, s , is also a concern when comparing damping fins with real textures. It is possible to make the spacing of the fins as small as the grid spacing in the spanwise direction, so that every grid point is part of a damping fin. In this pathological case spanwise velocity is strongly damped everywhere in the flow up to the height of the fins. By using such very closely spaced damping fins of sufficient height, it is possible to completely eliminate the spot and preserve laminar flow. However, real fins or riblets with very small spacings (compared to their height) behave essentially like a flat wall at the fin tops; such a flat wall is useless for damping turbulence. The spanwise damping fin results presented here are for cases which represent realistic geometries for real textures, and it is understood that such damping fins should only be compared to similarly sized realistic solid geometries.

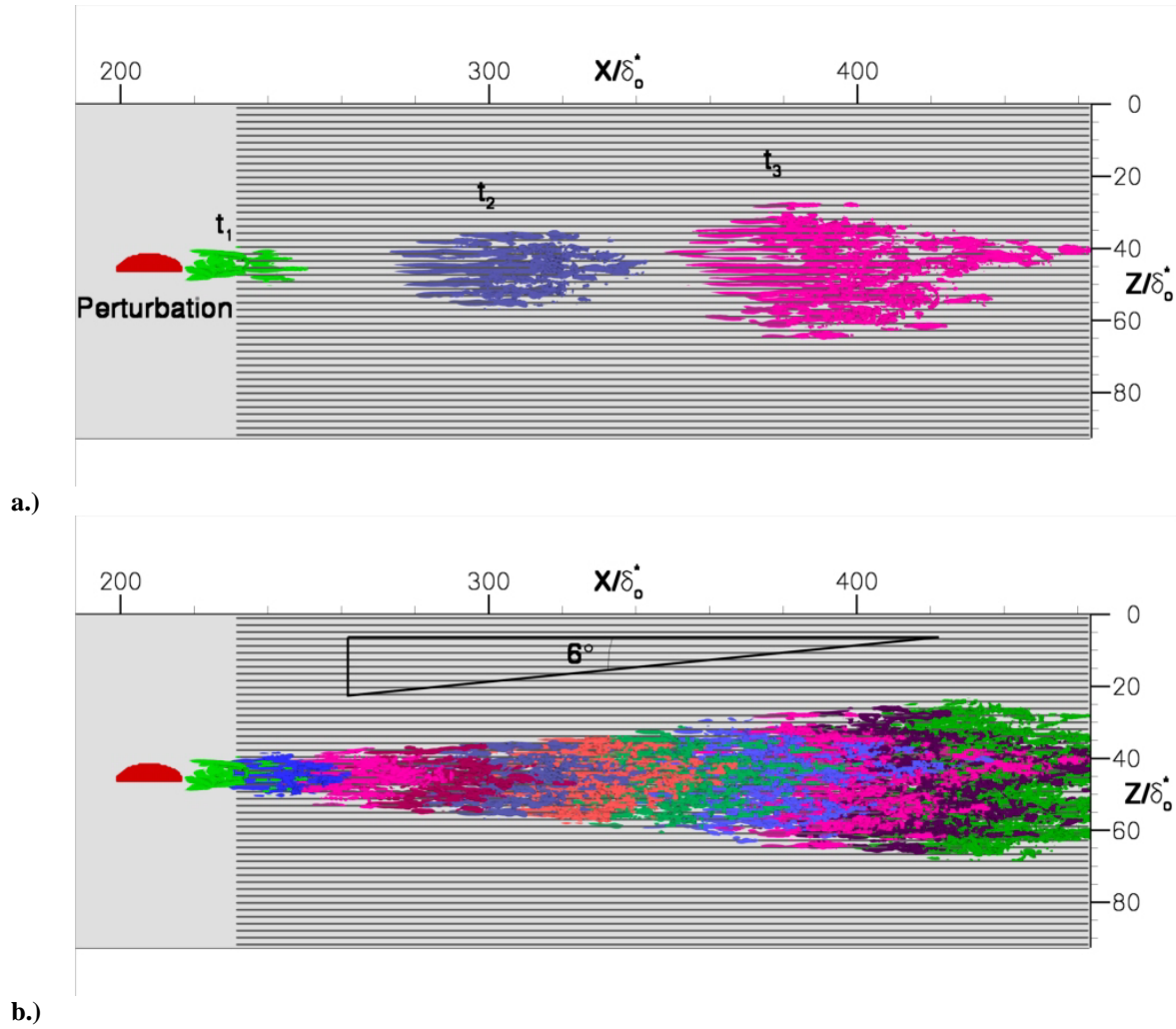


Figure 12. a.) Top view of turbulent spot over spanwise damping fins with $s = 1.93 \delta_0^*$ and $h = 0.46 \delta_0^*$, drawn with isosurfaces of enstrophy at the value of $0.756 U_\infty/\delta_0^*$ and shown at $t_1 = 64.5 \delta_0^*/U_\infty$, $t_2 = 208.4 \delta_0^*/U_\infty$, and $t_3 = 347.4 \delta_0^*/U_\infty$. This run used $512 \times 64 \times 128$ spectral modes in the x , y , and z directions, respectively. b.) Isosurfaces (same definition as above) shown for multiple time steps simultaneously, in order to illustrate spot spreading angle.

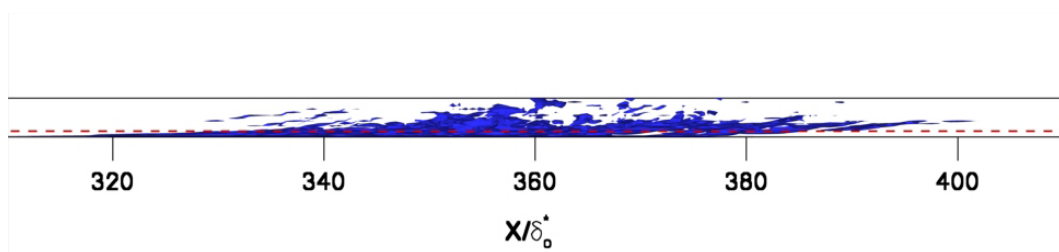


Figure 13. Side view of turbulent spot over damping fins, drawn with isosurfaces of enstrophy at the value of $0.756 U_\infty/\delta_0^*$ and shown at $t = 277.9 \delta_0^*/U_\infty$. The red dashed line indicates the height of the spanwise damping fins. Note that only the 20% of the domain closest to the bottom wall is shown. This run used $512 \times 64 \times 128$ spectral modes in the x , y , and z directions, respectively.

Figure 12 shows results for a typical spanwise damping fin case. The domain and perturbation are identical to that described previously for the flat wall case, and the spot is defined in the same way (the same isosurface of enstrophy). Here (as in the first flat wall case) $512 \times 64 \times 128$ spectral modes were used in the x , y , and z directions, respectively. As can be seen, the spot spreading angle is somewhat lower, but has not been hugely altered. However, comparing Fig. 12a to Fig 6b, it appears that the turbulence inside the spot is less intense in the case with the spanwise damping fins than in the flat wall case. Note that these are top-down views of the 3D flowfield, not 2D slices, so it is not simply a matter of the particular plane at which the spot is sliced. This apparently weaker turbulence inside the spot can be observed with isosurfaces drawn at other values of enstrophy, so it is not simply an artifact of this particular enstrophy value. When comparing Fig. 12b to Fig. 8, another interesting effect of the damping fins can be observed. In Fig. 8, the flat wall case, there is no apparent pattern to the spreading of the spot, other than that it spreads at a reasonably constant rate. However, in Fig. 12b, the spanwise edge of the spot seems to make discrete jumps from one fin location to the next. The spanwise growth of the spot as it travels downstream appears stairstepped, rather than mostly linear as is the case with the flat wall spot.

A side view of the spot is seen in Fig. 13, for comparison to Fig. 7 for the flat wall case. The red dashed line indicates the height of the damping fins. The majority of the turbulence is located above the height of the damping fins. The spot is nearly identical in length to the flat wall spot, and has the same distinct overhang at the leading edge. However, the flat wall spot extends farther from the wall and is thicker and better defined. This again indicates that the turbulence is being weakened by the damping fins, as would be expected.

In order to examine more closely spaced fins with sufficient resolution, a case was run with double the spanwise resolution ($512 \times 64 \times 256$ spectral modes in the x , y , and z directions, respectively). The domain is the same as for the cases described above, as is the height of the damping fins used ($h = 0.460 \delta_o^*$). For this case, the spacing of the damping fins was reduced to $s = 0.965 \delta_o^*$. This gives a height to spacing ratio of 0.48. Note that this is not an unrealistic spacing for real fins or riblets. Goldstein, Handler, and Sirovich⁹ found turbulent drag reduction for riblets with $h/s = 0.8$, and many experiments have found that optimal riblets for drag reduction have a ratio $h/s \approx 1$. Figure 14 shows a top-down view for this case, comparable to Fig. 9 for the higher-resolution flat wall case. At this spacing, the damping fins almost completely stop the spreading of the spot. The spot grows initially, but then stops spreading and simply convects downstream. Inside the spot, the turbulence appears far weaker than for the flat wall case. Figure 15 is a zy slice, taken at a location $359.56 \delta_o^*$ from the leading edge of the plate, showing contours of enstrophy, at $t = 347.4 \delta_o^*/U_\infty$. This figure is comparable to Fig. 10, except that it is taken one time interval earlier. (Data are output at intervals of $34.7 \delta_o^*/U_\infty$.) The spot over these closely spaced fins is so small (it not only spreads far less, it is shorter as well) that using the data on this plane from the time interval shown in Fig. 10 misses most of the spot. In both Fig. 10 and Fig. 15 the spot is shown at its widest extent.

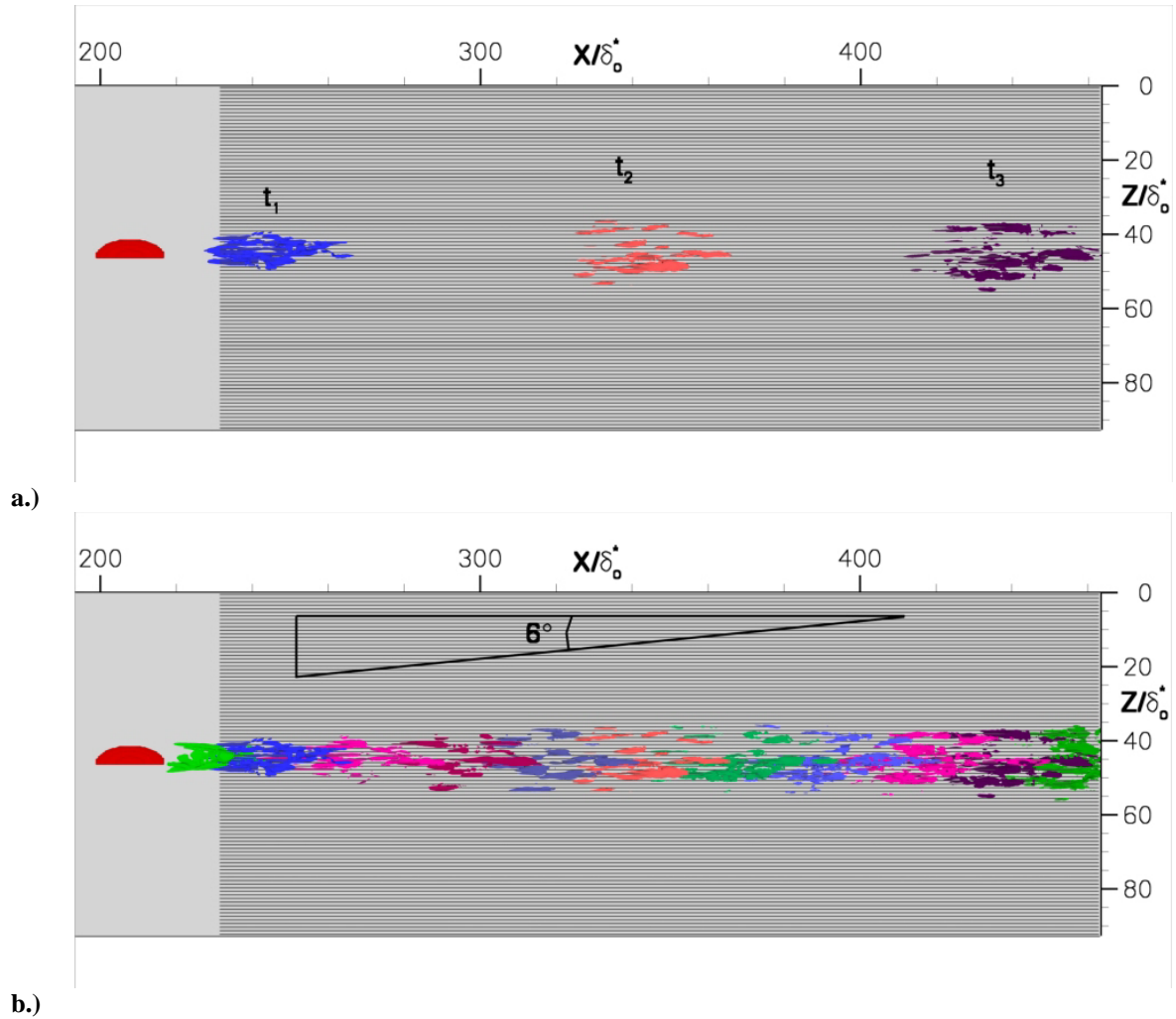


Figure 14. a.) Top view of turbulent spot over spanwise damping fins with $s = 0.965 \delta_0^*$ and $h = 0.46 \delta_0^*$, drawn with isosurfaces of enstrophy at the value of $0.756 U_\infty/\delta_0^*$ and shown at $t_1 = 64.5 \delta_0^*/U_\infty$, $t_2 = 208.4 \delta_0^*/U_\infty$, and $t_3 = 347.4 \delta_0^*/U_\infty$. This run used $512 \times 64 \times 256$ spectral modes in the x , y , and z directions, respectively. b.) Isosurfaces (same definition as above) shown for multiple time steps simultaneously, in order to illustrate spot spreading angle.

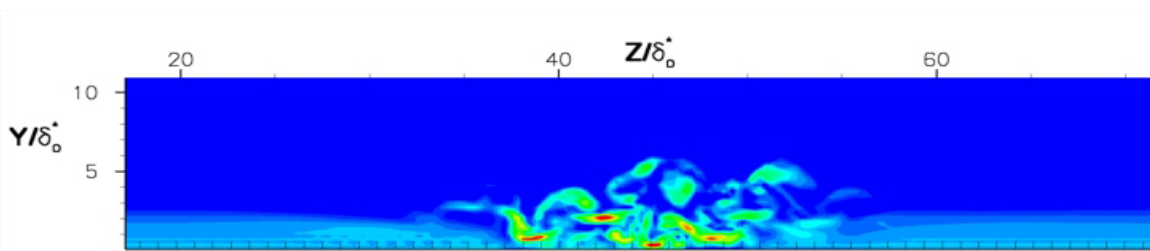


Figure 15. Contours of enstrophy on a zy plane located $359.56 \delta_0^*$ from the leading edge of the plate, at time $t = 347.4 \delta_0^*/U_\infty$. This run used $512 \times 64 \times 256$ spectral modes in the x , y , and z directions, respectively. One clearly sees the decreased spreading of the spot due to the damping fins.

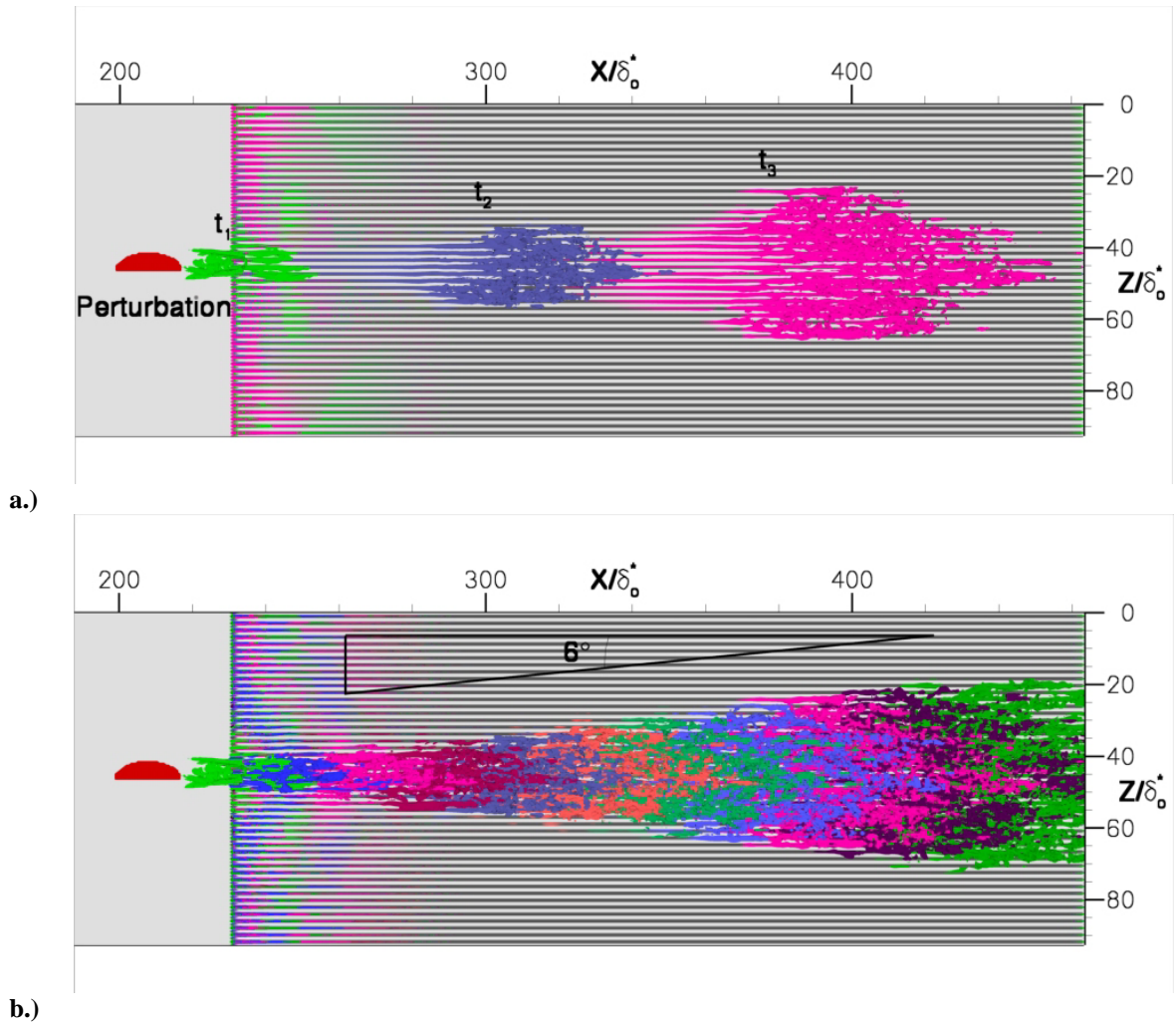


Figure 16. a.) Top view of turbulent spot over real fins with $s = 1.93 \delta_0^*$ and $h = 0.46 \delta_0^*$, drawn with isosurfaces of enstrophy at the value of $0.756 U_\infty/\delta_0^*$ and shown at $t_1 = 64.5 \delta_0^*/U_\infty$, $t_2 = 208.4 \delta_0^*/U_\infty$, and $t_3 = 347.4 \delta_0^*/U_\infty$. This run used $512 \times 64 \times 128$ spectral modes in the x, y, and z directions, respectively. b.) Isosurfaces (same definition as above) shown for multiple time steps simultaneously, in order to illustrate spot spreading angle.

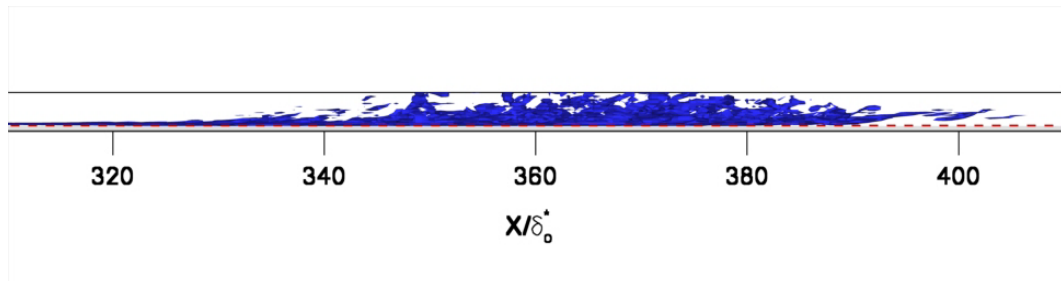


Figure 17. Side view of turbulent spot over real fins, drawn with isosurfaces of enstrophy at the value of $0.756 U_\infty/\delta_0^*$ and shown at $t = 277.9 \delta_0^*/U_\infty$. The red dashed line indicates the height of the fins. Note that only the 20% of the domain closest to the bottom wall is shown. This run used $512 \times 64 \times 128$ spectral modes in the x, y, and z directions, respectively.

D. Real Fins

We next examine physically realistic fins. As described before, these fins enforce both no-slip and no-through conditions on the velocity. As described earlier, with damping fins the same relaxed profile can be used for any combination of fin height and spacing, since the damping fins have no effect on the flow until it is perturbed. Real fins, however, significantly alter the laminar boundary layer profile in the region near the wall, and thus relaxation to a steady laminar state was performed with the fins already in the flow.

Figure 16 shows results for a typical case with real fins. The domain, grid, and perturbation are the same as for the flat wall case described first ($512 \times 64 \times 128$ spectral modes), and the spot is defined in the same way. The spot can still be clearly seen with this enstrophy isosurface, but there are also regions with this relatively high value of enstrophy that are not associated with the spot. High enstrophy is present in the region where the fins begin, and for some distance downstream. The spot appears more symmetric than in the spanwise damping fins case. The wake of the spot extends far behind the spot, and its interaction with the fins leads to high enstrophy in this region as well. Inside the spot, the turbulence appears weaker than in the flat wall case, but stronger than for the similarly spanwise damping fins case.

Figure 17 is a side view of the spot. The spot is the same length as in the flat wall and damping fin cases, and again the majority of the spot is located above the height of the fins. The overhang is once again present. The turbulent region of the spot extends farther from the wall than in the damping fins case. As in the top down view, the turbulence appears slightly weaker than in the flat wall case.

As in the spanwise damping fin and flat wall cases, a run was recently completed with double the spanwise resolution ($512 \times 64 \times 256$ spectral modes). Once again, the domain and perturbation are the same as for all previous runs. As in the spanwise damping fins case, the extra spanwise resolution allowed for the simulation of more closely spaced fins ($s = 0.965 \delta_o^*$). As discussed in the previous section, this is a reasonable fin spacing. As with the previous fin cases, the enstrophy isosurfaces show not only the spot but also the high enstrophy region near the start of the fins. Comparing Fig. 18a. with Fig. 9a. the turbulence inside the spot appears a little weaker than the turbulence inside the flat wall spot. Comparing Fig. 18b. with Fig. 9b, it appears that the spot spreads slightly slower over the fins than over the flat wall.

A zy slice, taken at a distance $359.56\delta_o^*$ from the leading edge of the plate, is displayed in Fig. 19. The figure shows contours of enstrophy, at time $t = 347.4 \delta_o^*/U_\infty$. This figure is comparable to Fig. 10 for the flat wall case, with both showing the same location at the same time. The regions of high enstrophy have been pushed up and away from the nominal wall location (at the base of the fins), as was discussed previously. As in the flat wall case, a multitude of turbulent structures can be seen, including many streamwise vortices. The spot extends well above the height of the fins.

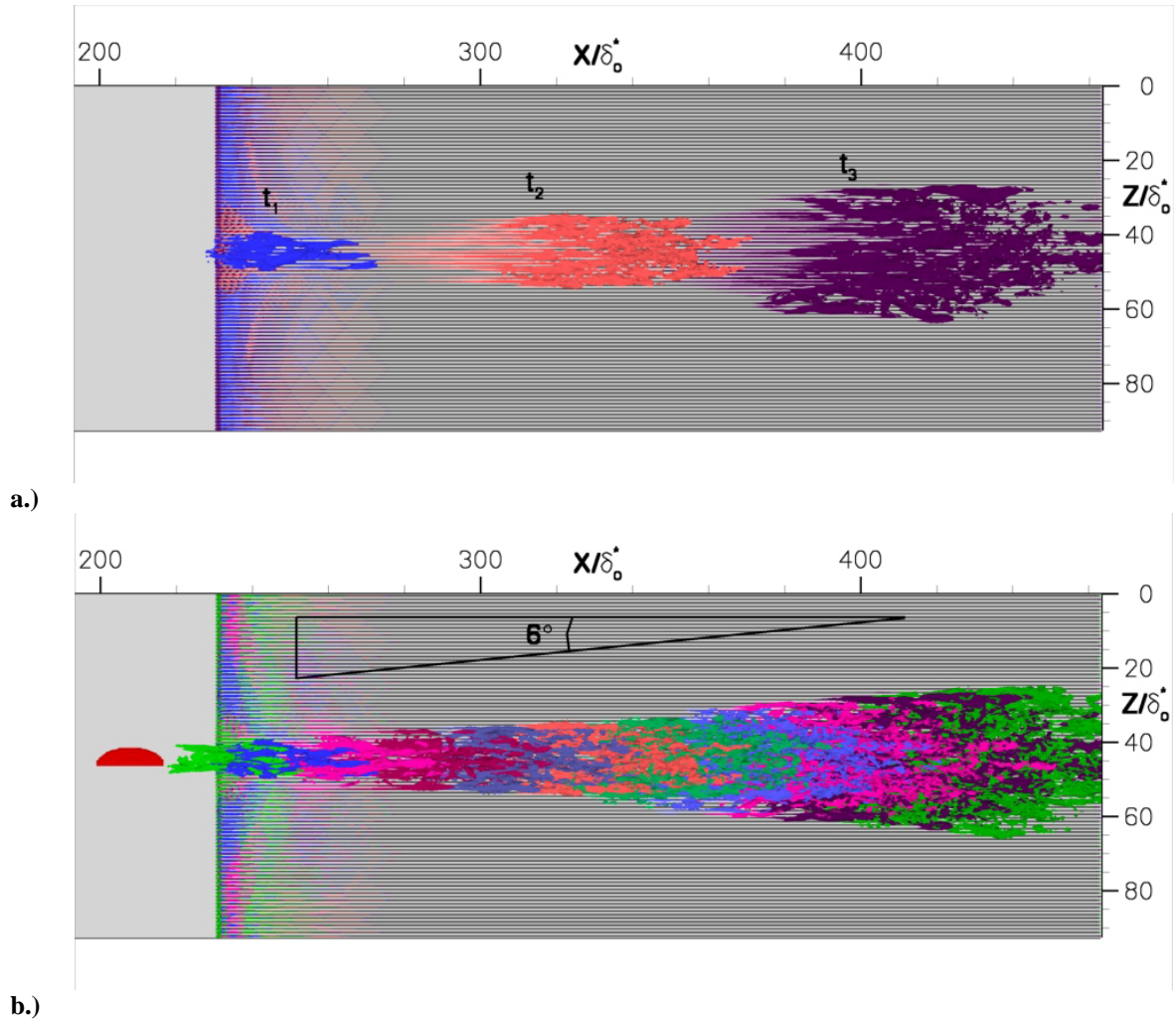


Figure 18. a.) Top view of turbulent spot over real fins with $s = 0.965 \delta_0^*$ and $h = 0.46 \delta_0^*$, drawn with isosurfaces of enstrophy at the value of $0.756 U_\infty/\delta_0^*$ and shown at $t_1 = 64.5 \delta_0^*/U_\infty$, $t_2 = 208.4 \delta_0^*/U_\infty$, and $t_3 = 347.4 \delta_0^*/U_\infty$. This run used $512 \times 64 \times 256$ spectral modes in the x, y, and z directions, respectively. b.) Isosurfaces (same definition as above) shown for multiple time steps simultaneously, in order to illustrate

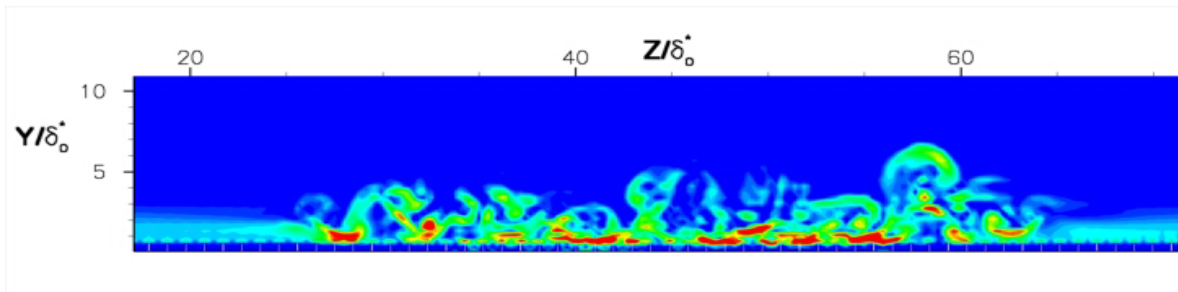


Figure 19. Contours of enstrophy on a zy plane located $359.56 \delta_0^*$ from the leading edge of the plate, at time $t = 381.2 \delta_0^*/U_\infty$. This run used $512 \times 64 \times 256$ spectral modes in the x, y, and z directions, respectively.

E. Riblets

With the aid of greater spanwise resolution, we have now begun to study triangular-shaped riblets. Figure 20 shows the results from one such case. The domain is the same as for all previous runs, and $512 \times 64 \times 256$ spectral modes were used in the x, y, and z directions, respectively. The riblets have a crest-to-crest spacing, s , of $1.930 \delta_0^*$

and height, h , of $0.46 \delta_0^*$. The height and spacing used here match those used for the damping fin case shown in Fig. 12 and the real fin case shown in Fig. 16. Those two cases were run with half the spanwise resolution used here however. Since each riblet requires a minimum of 8 collocation points in the spanwise direction, we have not yet been able to simulate riblets with the $0.965 \delta_0^*$ spacing used by the most closely spaced real and damping fin cases. In order to compare to the fin cases (where the only relevant parameters are fin height and spacing), we have made these riblets as close to isosceles triangles as the grid allows (so that once again height and spacing are the only important parameters). In general, it is not required that riblets be truly triangular, and cusped riblets are often used in experiments, and in the future higher resolution cases will allow us to simulate more complicated riblet geometries. In Fig. 20, high enstrophy is present not only in the region of the spot, but also in the region near the leading edge of the riblets, as was the case with the real fins. As in the fin cases, the spot edge seems to jump from one riblet crest to the next, rather than spread in a simple, roughly linear way, characteristic of the flat wall case.

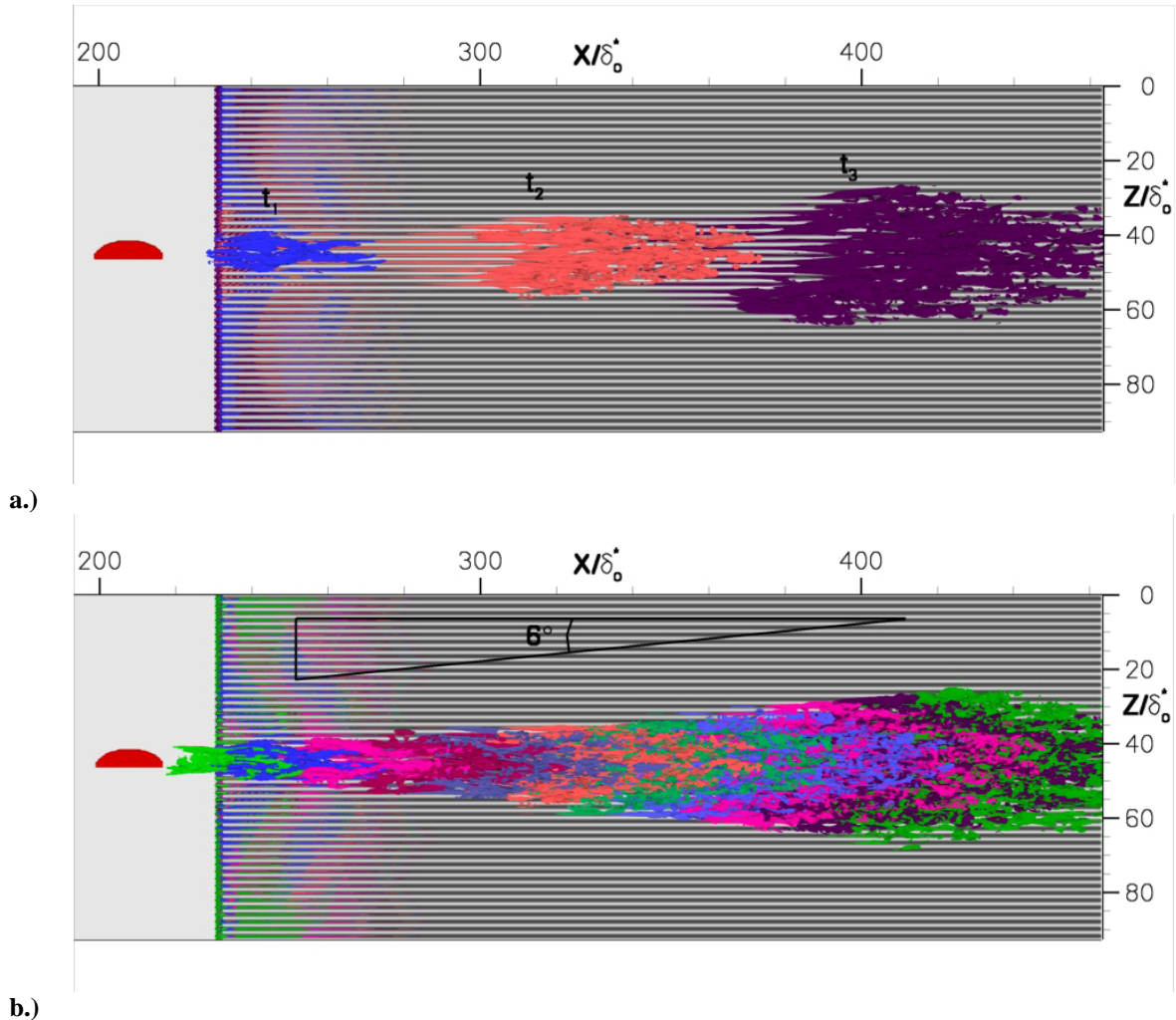


Figure 20. a.) Top view of turbulent spot over riblets with $s = 1.930 \delta_0^*$ and $h = 0.46 \delta_0^*$, drawn with isosurfaces of enstrophy at the value of $0.756 U_\infty/\delta_0^*$ and shown at $t_1 = 64.5 \delta_0^*/U_\infty$, $t_2 = 208.4 \delta_0^*/U_\infty$, and $t_3 = 347.4 \delta_0^*/U_\infty$. This run used $512 \times 64 \times 256$ spectral modes in the x , y , and z directions, respectively. b.) Isosurfaces (same definition as above) shown for multiple time steps simultaneously.

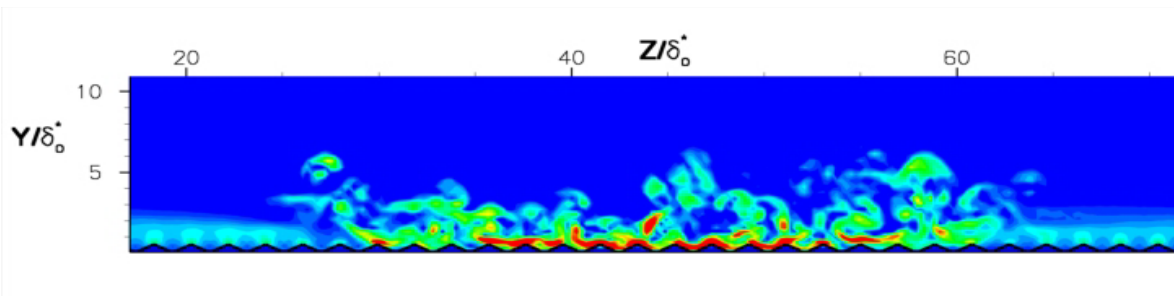


Figure 21. Contours of enstrophy on a zy plane located $360\delta_o^*$ from the leading edge of the plate, at time $t = 381.2 \delta_o^*/U_\infty$. This run used $512 \times 64 \times 256$ spectral modes in the x , y , and z directions, respectively. Riblets indicated with black lines.

Figure 21 is a zy slice, taken at a distance $359.56\delta_o^*$ from the leading edge of the plate, showing contours of enstrophy at time $t = 347.4 \delta_o^*/U_\infty$. This figure is comparable to Fig. 10 for the flat wall case, with both showing the same location at the same time. The riblets themselves can be seen near the bottom wall. Away from the spot edge, regions of increased enstrophy ride along the riblet crests, as seen previously with the real fins. In the center of the spot, however, regions of strong enstrophy are present in the riblet valleys, well below the height of the riblet crests.

F. Spreading Angle Comparisons

In order to compare spreading angles from one case to another, a consistent method must be used to define the spot. Here we have used two quantities to define the spot, enstrophy and vertical velocity. The spanwise edge of the spot is defined as the location farthest from the centerline (at any value of x and y) at which the given quantity (enstrophy or vertical velocity) is greater than or equal to a specific cutoff value. The (x, y, z) location of the spanwise edge is recorded at set time intervals, for each cutoff value of each quantity. Two cutoff values were used for enstrophy and one for vertical velocity. These cutoff values were chosen empirically by observing which isosurfaces allowed the spot to be seen most clearly. The cutoff values for enstrophy were $0.864 U_\infty/\delta_o^*$ and $0.971 U_\infty/\delta_o^*$. The cutoff value for vertical velocity was $0.08 U_\infty$. The cutoffs chosen are several times larger than the highest values of enstrophy and vertical velocity present in the Blasius profile. One problem with this method is the fact that in the cases with real fins, high enstrophy values (above all three cutoffs used) are present in the region of the beginning of the fins, far from the spot. Fortunately, this enstrophy extends only a relatively small distance downstream. To account for this, the definition of the spanwise edge is modified slightly, and high enstrophy values far from the centerline are ignored unless they are a set distance downstream of the beginning of the fins. This means that a spreading angle cannot be calculated for the growing pre-turbulent spot at very early time steps. This is not really a problem, because the spot has not taken on its arrowhead shape yet at these early stages, and its shape is presumably still dependent on the specific perturbation used. For the present work, we are primarily interested in the characteristics of the spot once it has achieved a self-similar shape, which occurs farther downstream.

Once the location of the spanwise edge has been determined at each time interval (for a specific cutoff value), linear regression is used to define the spreading angle. A plot is made of the spanwise extent of the spot versus the streamwise location of the spanwise edge, with one data point being recorded for each interval at which data is output. There are two methods of linear regression used here. In the first method, there is no virtual origin for the spreading angle, and the trendline is forced to pass through the origin (the origin is defined as the x, z location of the center of the perturbation). In the second method, the trendline is not forced to pass through the origin, and a virtual origin is calculated along with the spreading angle. In the first method, only the magnitude of the spanwise extent is used for the calculations, not whether it is on the left or right side of the spot. (In this section the left and right side of the spot will be defined as if the observer were looking downstream, parallel to the freestream. Then the left side of the spot would be on the left hand side of the observer, and the right side of the spot would be on the right hand side of the observer.) In the second method, a spreading angle and virtual origin are calculated separately for the left and right sides of the spot, and then those values are averaged to compute a single spreading angle and virtual origin for the spot. See Fig. 1 for a schematic view showing a turbulent spot with the origin for the spreading angle defined as the center of the perturbation, and Fig. 22 for a schematic view with a virtual origin.

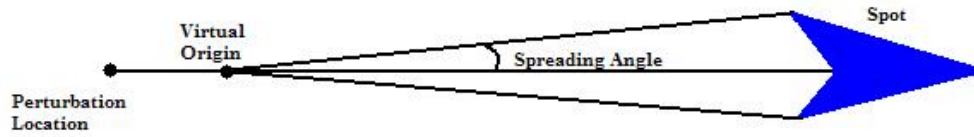


Figure 22. Schematic top view of a turbulent spot with a virtual origin for the spreading angle.

Since for this work we are interested in the behavior of the spot once it becomes reasonably self-similar, in both methods the linear regression is based on the data points from only the final 1/3 of the run (after $t = 277.9 \delta_0^*/U_\infty$). This also largely eliminates the problem of enstrophy from the fins not associated with the spot.

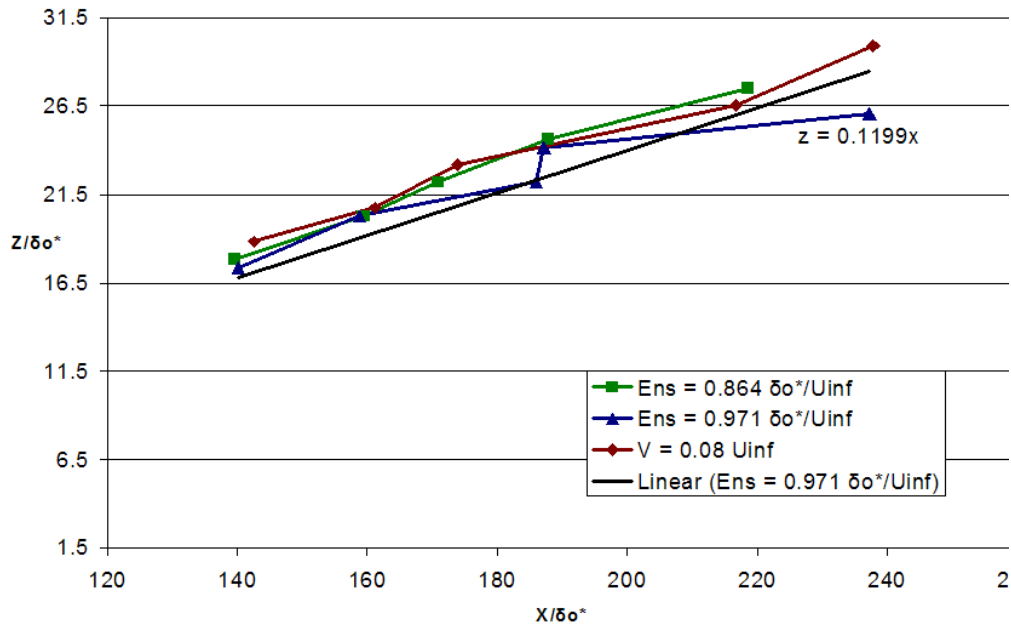


Figure 23. Example showing calculation of spreading angle for the flat wall case, with no virtual origin. Data points shown for all three cutoffs and trendline shown only for enstrophy cutoff of $0.971 U_\infty/\delta_0^*$.

Table 1. Spreading angle (in degrees) for various cases. Angles were calculated without using a virtual origin. All cases shown here were run with $512 \times 64 \times 128$ spectral modes in the x, y, and z directions, respectively.

Cutoff	Flat Wall	Real Fins ($h = 0.463\delta_0^*$)			Damping Fins ($h = 0.463\delta_0^*$)		
		$s=1.930\delta_0^*$	$s=2.895\delta_0^*$	$s=3.860\delta_0^*$	$s=1.930\delta_0^*$	$s=2.895\delta_0^*$	$s=3.860\delta_0^*$
Enstrophy = $0.864 \delta_0^*/U_\infty$	7.3	6.8	7.1	NA	5.8	6.7	7.2
Enstrophy = $0.971 \delta_0^*/U_\infty$	6.8	6.7	6.8	6.8	5.5	6.6	7.1
$V = 0.08 U_\infty$	7.3	6.8	6.9	7.0	6.0	6.6	7.2
Average	7.1	6.8	7.0	6.9	5.8	6.6	7.1

Table 2. Spreading angle (in degrees) for various cases. Angles were calculated without using a virtual origin. All cases shown here were run with 512×64×256 spectral modes in the x, y, and z directions, respectively.

Cutoff	Flat Wall	Real Fins	Damping Fins	Riblets
		$h=0.463\delta_o^*$, $s=0.965\delta_o^*$	$h=0.463\delta_o^*$, $s=0.965\delta_o^*$	$h=0.463\delta_o^*$, $s=0.965\delta_o^*$
Enstrophy = $0.864 \delta_o^*/U_\infty$	5.7	5.1	2.5	5.1
Enstrophy = $0.971 \delta_o^*/U_\infty$	5.7	5.1	2.2	5.1
$V = 0.08 U_\infty$	5.8	5.1	2.8	5.3
Average	5.7	5.1	2.5	5.2

Figure 23 shows an example of a typical trendline for the first method (no virtual origin). Tables 1 and 2 above list the spreading angles for all cases considered, for each cutoff value of enstrophy and vertical velocity, calculated with no virtual origin. Table 1 shows the results of the runs with 512×64×128 spectral modes and Table 2 shows the results for runs with 512×64×256 spectral modes. The flat wall case was run with both resolutions.

Several trends are easily noticed. First, in almost all cases the angle is slightly higher at the lower cutoff value of enstrophy than at the higher cutoff value. This is an inevitable effect of the method used to calculate the angle. The spanwise edge is defined as the farthest point from the centerline at which the quantity (enstrophy or vertical velocity) is greater than or equal to the cutoff value. Thus, any point that meets the higher cutoff by definition meets the lower cutoff as well. So, the farthest spanwise extent will always be at least slightly larger for the lower cutoff value. It is still possible to have a lower angle for the lower cutoff however. This can happen if the location of farthest spanwise extent for the higher cutoff is significantly upstream of the location of farthest extent for the lower cutoff. Then, even though the spanwise extent of the spot is greater for the lower cutoff value, the spreading angle is actually calculated as smaller than for the higher cutoff value. Singer⁷ encountered this issue of jumps in the streamwise position of the spanwise edge of the spot as well.

Comparing the lower resolution fin cases to the flat wall case (Table 1), a slight decrease in the spreading angle can be noticed for all fin cases compared to the flat wall case, for all cutoff values. By all measures the spreading angle was lowest for the lowest spacing, and increased as spacing increased.

The spreading angle for the higher resolution fin case ($s = 0.965\delta_o^*$) also decreased compared to the flat wall spot at the comparable resolution (Table 2). Based on the values for the three cutoffs, the average drop in spreading angle for the closely spaced fin case was 0.6°, or 11% of the flat wall value.

Like the real fins, the damping fins are more effective when they are more closely spaced. Examining the lower resolution cases first, the most widely spaced damping fins ($s = 3.860\delta_o^*$) are seen to have almost no effect on the spreading angle. The $s = 2.895\delta_o^*$ damping fins have some effect on the spreading angle, but it is not large. The $s = 1.930\delta_o^*$ damping fins, however, have a significant effect. Averaging over all the cutoffs, we get a drop of 1.4° (or 19% of the flat wall value) for these damping fins compared to the flat wall case at the same resolution.

The higher resolution case with very closely spaced damping fins ($s = 0.965\delta_o^*$) shows an even larger drop in spreading angle. Once again averaging over all cutoffs, we find an average drop of 3.2°, or 56% of the flat wall value. In fact, based on Fig. 14b., these damping fins may completely stop the spot from spreading. The initial perturbation grows, but then appears to stop spreading and simply convects downstream.

Finally, for the riblet case the average drop in spreading angle is approximately the same as for the real fin case. The average decrease in spreading angle over the riblets is 0.6° (10% of the flat wall value).

Table 3. Spreading angle (in degrees) for the cases shown to be most effective with the previous method. Angles were calculated from a virtual origin, rather than from the center of the perturbation. The location of the virtual origin, with respect to the center of the perturbation, is listed for each case, with units of δ_o^* . A positive number for VO indicates that the virtual origin was downstream of the center of the perturbation, and a negative number indicates the virtual origin was upstream. All cases shown here were run with $512 \times 64 \times 128$ spectral modes in the x, y, and z directions, respectively.

Cutoff	Flat Wall		Real Fins		Damping Fins	
	VO	Alpha	$h = 0.463\delta_o^*, s = 1.930\delta_o^*$			
			VO	Alpha	VO	Alpha
Enstrophy = $0.864 \delta_o^*/U_\infty$	-10	6.8	37	8.2	-40.7	4.7
Enstrophy = $0.971 \delta_o^*/U_\infty$	-48	5.6	67	10.0	9.5	5.7
$V = 0.08 U_\infty$	-58	5.5	50	9.0	-1.8	5.5
Average	-39	5.9	51	9.1	-11.0	5.3

Table 4. Spreading angle (in degrees) for the enhanced resolution cases shown to be most effective with the previous method. Angles were calculated from a virtual origin, rather than from the center of the perturbation. The location of the virtual origin, with respect to the center of the perturbation, is listed for each case, with units of δ_o^* . All cases shown here were run with $512 \times 64 \times 256$ spectral modes in the x, y, and z directions, respectively.

Cutoff	Flat Wall		Real Fins	
	VO	Alpha	$h = 0.463\delta_o^*, s = 0.965\delta_o^*$	
			VO	Alpha
Enstrophy = $0.864 \delta_o^*/U_\infty$	26	6.8	13.9	5.2
Enstrophy = $0.971 \delta_o^*/U_\infty$	31	7.0	1.3	5.0
$V = 0.08 U_\infty$	21	6.4	16.7	5.4
Average	26	6.7	10.6	5.2
Cutoff	Damping Fins		Riblets	
	$h = 0.463\delta_o^*, s = 0.965\delta_o^*$			
	VO	Alpha	VO	Alpha
Enstrophy = $0.864 \delta_o^*/U_\infty$	-20	1.9	27.5	6.7
Enstrophy = $0.971 \delta_o^*/U_\infty$	-30	1.8	2.8	5.7
$V = 0.08 U_\infty$	-129	1.5	29.3	6.5
Average	-60	1.7	19.9	6.3

Now, we examine the spreading angle results based on the second method, where a virtual origin is calculated for each case. Only the flat wall case, riblet case, and the most closely spaced real and damping fin cases for each resolution were examined with this method (the $s = 1.930\delta_o^*$ real and damping fins for the cases with $512 \times 64 \times 128$ spectral modes, and the $s = 0.965\delta_o^*$ real and damping fins for the cases with $512 \times 64 \times 256$ spectral modes).

In Table 3, the spreading angle is seen to be significantly higher for the lower resolution fins case than for the corresponding flat wall case (an increase of 3.1° when averaged over the three cutoffs). However, the virtual origin

has moved downstream by an average value of $90\delta_o^*$ from its location in the flat wall case. Thus, the angle is calculated to be larger for the fin case, but the spot has actually *not* spread as much because the virtual origin is moved so far downstream. For the lower resolution damping fins case, the average spreading angle is lower, *and* the virtual origin has moved downstream from its original location in the flat wall case.

In the higher resolution runs we see that both the real fins and the riblets help to constrain spreading, in agreement with previous conclusions. The spot over the $s = 0.965 \delta_o^*$ real fins has an average spreading angle which is reduced by 1.5° , or 23% of the flat wall value. Furthermore, the virtual origin has moved downstream from its original location, so not only is the spot spreading with a lower angle, but the location from which that angle is measured is farther downstream than in the flat wall case. This shows clearly that the closely spaced real fins are having the desired effect. The riblets are not as closely spaced as the fins, but they are still able to reduce the spreading angle by 0.5° (7% of the flat wall value), while at the same time moving the virtual origin slightly downstream from its location in the flat wall case.

Finally, the $s = 0.965 \delta_o^*$ damping fins are once again shown to be extremely effective at constraining spot spreading. Although they move the virtual origin upstream of its location from the flat wall case, they cut the spreading angle by 5.0° (74% of the flat wall value).

G. Effect of Suction Wall on Results

It is not completely clear how much of an effect the suction wall method had on the results. There are several issues concerning the suction wall. The first is exactly what vertical velocity to force when a textured surface is being modeled instead of a flat wall, since there is not an analytic solution for the laminar boundary layer profile over riblets or fins. In the present work the textures are small compared to the boundary layer thickness, and they should have negligible effect on the flow outside the boundary layer, especially the vertical velocity in the far field. Thus, in this case, we can simply use the vertical velocity from the Blasius solution.

The second issue involves the spot itself. It is true that our spots only tend to occupy roughly the lower third of the domain, yet the Blasius solution is for laminar flow over a flat plate. The increase in displacement thickness with streamwise distance, $d\delta^*/dx$, is very different for a turbulent boundary layer than for a laminar one, and it is this value which determines the vertical velocity far from the plate. If the boundary layer was fully turbulent, we could just use the power law expression for a turbulent boundary layer. With a spot however, turbulence is only present over part of the planform area of the plate, and the location of the spot moves over time. Even if a vertical velocity field could be found for a “generic” spot, it would still be highly time dependent. We are still searching for solutions to this issue. One possible solution is to adapt the suction wall in some way, by changing over time the desired vertical velocity at each location, until some specific criteria is met. For example, the suction wall might be made to adapt until the streamwise velocity at all points on a horizontal plane well above the boundary layer edge was very close to U_∞ . Alternatively, we could utilize a regular boundary layer code.

The primary concerns of this study were the downstream growth and spreading of the spot, as opposed to the detailed structures within the spot. The spreading angle and propagation speeds found for the flat wall case agree reasonably well with most of the experimental and DNS results discussed previously. It seems acceptable, then, to assume that the current method also does a reasonable job of modeling the growth and spreading of the spots over the small textured surfaces located deep in the boundary layer, thus allowing us to meaningfully analyze the effects of the textures on these quantities.

H. Conclusions and Future Work

More work must still be done before we can fully characterize the effects of textures on the growth and spreading of spots. Simulations must be run with greater resolution, to confirm grid independence, and because more closely spaced riblets and fins require greater spanwise resolution. The domain may also be lengthened significantly. The spot growth seen in the flat wall cases here is comparable to that seen by Singer⁷, but we would like to increase our domain size and Reynolds number in order to examine the effects of textures on spots at the experimental Reynolds numbers.

However, the results seen so far are quite encouraging. The spanwise damping fins proved extremely effective for constraining spot growth. More importantly, real fins with a height to spacing ratio of ~ 0.5 were able to reduce spreading angle by 10%-20% (depending on which method of calculation is used), and riblets with height to spacing ratio of ~ 0.25 were able to reduce spreading by 7%-10%. Optimal riblets for turbulent drag reduction have height to

spacing ratios of ~ 1 . It is possible, then, that when we are able to simulate real fins and riblets with these smaller spacings, we will see further improved reduction of spot spreading.

Acknowledgments

We would like to thank AFOSR for support through grant FA 9550-05-1-0176. We would also like to thank Dr. Robert Handler for his assistance throughout the process.

References

- ¹H. W. Emmons, "The Laminar-Turbulent Transition in a Boundary Layer - Part I," *J. Aeronautical Sciences*, Vol. 18, No. 7, July 1951, pp. 490-498
- ²G. B. Schubauer and P. S. Klebanoff, "Contributions to the Mechanics of Boundary-Layer Transition," NACA TN-3489, 1955.
- ³J. Wygnanski, M. Sokolov and D. Friedman, "On a Turbulent 'Spot' in a Laminar Boundary Layer," *J. Fluid Mechanics*, Vol. 78, 1976, pp. 785-819.
- ⁴J. Amini and G. Lespinard, "Experimental Study of an 'Insipient Spot' in a Transitional Boundary Layer," *Physics of Fluids*, Vol. 25, No. 10, Oct. 1982, pp. 1743-1750.
- ⁵D. Henningson, P. Spalart, and J. Kim, "Numerical Simulations of Turbulent Spots in Plane Poiseuille and Boundary Layer Flow," *Physics of Fluids*, Vol. 30, No. 10, Oct. 1987, pp. 2914-2917.
- ⁶B. Singer and R. Joslin, "Metamorphosis of a Hairpin Vortex into a Young Turbulent Spot," *Physics of Fluids*, Vol. 6, No. 11, Nov. 1994, pp. 3724-3736.
- ⁷B. Singer, "Characteristics of a Young Turbulent Spot," *Physics of Fluids*, Vol. 8, No. 2, Feb. 1996, pp. 509-521.
- ⁸E. Coustols and A. M. Savill, "Turbulent Skin-Friction Drag Reduction by Active and Passive Means: Parts 1 and 2," Special Course on Skin-Friction Drag Reduction, pp. 8-1 to 8-55, March 2-6, 1992 in AGARD Report 768.
- ⁹D. B. Goldstein, R. Handler, and L. Sirovich, "Direct Numerical Simulation of Turbulent Flow Over a Modeled Riblet Covered Surface," *J. Fluid Mechanics*, Vol. 302, No. 10, 1995, pp. 333-376.
- ¹⁰D. B. Goldstein and T.-C. Tuan, "Secondary Flow Induced by Riblets," *J. Fluid Mechanics*, Vol. 363, 1996, pp. 115-151.
- ¹¹D. B. Goldstein, R. Handler, and L. Sirovich, "Modeling a No-Slip Flow Boundary with an External Force Field," *J. Comp. Phys.*, Vol. 105, 1993, pp. 354-366.
- ¹²J. Kim, P. Moin, and R. Moser, "Turbulence Statistics in Fully Developed Channel Flow at Low Reynolds Number," *J. Fluid Mechanics*, Vol. 177, 1987, pp. 133-166
- ¹³R. A. Handler, E. W. Hendricks, and R. I. Leighton, "Low Reynolds Number Calculation of Turbulent Channel Flow: A General Discussion," NRL Memorandum Report 6410, 1989, pp. 1-103.
- ¹⁴D. Goldstein, J. Cohen and V. Levinski, "DNS of Hairpin Vortex Formation in Poiseuille Flow Due to Two-hole Suction," Presented at 3rd AFOSR Int. Conf. on DNS and LES, Arlington, TX, Aug. 2001
- ¹⁵F. M. White, *Viscous Fluid Flow*, 2nd ed., McGraw Hill, 1991, Chap. 4.